

Two-stage deep learning framework for the restoration of incomplete-ring PET images

Yeqi Fang¹ and Rong Zhou²

College of Physics, Sichuan University, Chengdu, 610065, China

E-mail: ¹fangyeqi@stu.scu.edu.cn

E-mail: ²rongzhou15@163.com

April 2025

Abstract. Positron Emission Tomography (PET) is an important molecular imaging tool widely used in medicine. Traditional PET systems rely on complete detector rings for full angular coverage and reliable data collection. However, incomplete-ring PET scanners have emerged due to hardware failures, cost constraints, or specific clinical needs. Standard reconstruction algorithms often suffer from performance degradation with these systems because of reduced data completeness and geometric inconsistencies. We present a two-stage deep-learning framework that, without incorporating any time-of-flight (TOF) information, restores high-quality images from data with about 50% missing coincidences—double the loss levels previously addressed by CNN-based methods. The pipeline operates in two stages: a projection-domain Attention U-Net first predicts the missing sections of the sinogram by leveraging spatial context from neighbouring slices, after which the completed data are reconstructed with OSEM algorithm and passed to a U-Net–diffusion module that removes residual artefacts while reinstating high-frequency detail. Using 206 brain volumes from a public dataset, the result shows that our model successfully preserves most anatomical structures and tracer distribution features with PSNR of 30.92 dB and SSIM of 0.9708. We also achieve higher inference speed, thus providing an effective solution for incomplete-ring PET imaging.

1. Introduction

Positron emission tomography (PET) is a powerful molecular imaging technique that provides quantitative visualization of metabolic processes within living tissue [1, 2, 3, 4, 5]. The fundamental principle is elegant but complex: a radiotracer introduces positrons that annihilate upon encountering electrons, and then produce pairs of 511keV photons traveling in opposing directions. The photon pairs are then detected by a pair of scintillation sensors, and each coincidence event will define a line-of-response (LOR). Traditional PET systems usually use complete 360° detector rings to maximize their sensitivity and angular coverage [1].

However, incomplete-ring systems have emerged from practical necessity rather than theoretical preference: they reduce costs and complexity, allow closer access

to patients in specialized applications like breast scanning or in-beam therapy monitoring [6], create "open" configurations that alleviate claustrophobia [7, 8], and enable novel applications such as dual-panel brain imaging systems [9]. The trade-off is severe—incomplete angular coverage creates gaps in projection data, turning reconstruction into an underdetermined problem. Missing angular views inevitably introduce artifacts and resolution non-uniformity [10, 6]. Even time-of-flight capabilities, which partially fix these problems, can't fully compensate for limited view angles [6, 8].

Researchers have investigated a lot of methods to achieve better and better incomplete-ring PET reconstruction. Analytical ways like filtered back-projection falter immediately—their assumption of complete data leads to pronounced streak artifacts [10]. Iterative approaches like maximum-likelihood expectation-maximization (MLEM) are better by modeling the acquisition process [11], but they still have artifacts along missing view directions [9]. Penalized likelihood methods incorporating prior constraints show promise, as Zhang *et al.* demonstrated by using high-quality prior images to enhance contrast recovery in a dual-panel head-and-neck PET system [9]. And sinogram completion approaches attempt to estimate or interpolate the absent projection data prior to reconstruction [12]. But these methods are still not enough to solve the fundamental problem.

Deep learning has shown remarkable success in many fields [13, 14, 15]. Regression-based networks have shown promise in low-dose PET denoising and partial data reconstruction [16] by learning direct mappings between degraded and high-quality images. Liu *et al.*'s U-Net approach to transform artifact-degraded partial-ring PET images [17] demonstrated initial success, but the model in this work is mainly targeted for mild data loss and training data didn't consider the context of sinograms. However, current available techniques have some drawbacks. For examples, while GAN approaches are good at generating visually compelling reconstructions, [18] they are unstable when training and often highly sensitive to hyperparameters, which limit their clinical use. Methods based on explicit likelihood modeling—like VAEs and flow-based approaches—offer solid theoretical foundations. But they usually lose details in reconstructed images and their low speeds also make them not suitable for clinical use. Model-based deep learning frameworks and generative models [19, 20] show promise but risk introducing hallucinated features—a dangerous proposition in medical imaging.

In this work we introduce a two-stage deep-learning framework that restores highly degraded partial-ring PET data and, for the first time, is validated under $> 50\%$ coincidence loss. Our contributions are four-fold: (1) we propose a five-channel slice-stacking strategy that fuses immediate spatial and axial neighbours in the sinogram, providing rich local context for projection restoration; (2) missing-angle gaps are reconstructed with an Attention U-Net specifically tuned for severe angular deficits, enabling the network to focus selectively on informative sinogram regions; (3) the resulting OSEM images are passed to a lightweight residual-diffusion module that iteratively synthesises high-frequency details while suppressing artefacts, thereby decoupling data completion from perceptual refinement; and (4) we establish the first

systematic benchmark on 206 public brain volumes with half the coincidences removed, demonstrating that our pipeline achieves 30.9 dB / 0.97 SSIM in image space and runs in < 2 s per image on a single GPU—surpassing existing partial-ring methods without hand-tuned regularisation.

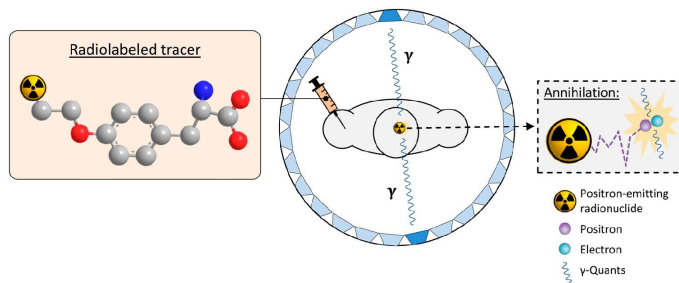


Figure 1. Principles of Positron Emission Tomography (PET) imaging [21].

The remainder of this thesis is organized as follows: **Section 2** provides an overview of PET and its basic physics like principles of coincidence detection, and the main problems caused by incomplete rings. We also summarize classical and modern reconstruction methods. **Section 3** presents our contribution in full: the simulation framework for complete and partial rings, the projection-completion Attention U-Net, the subsequent OSEM reconstruction, and the diffusion-based image-refinement module, together with implementation and training details. **Section 4** reports quantitative and qualitative evaluations on 206 brain volumes under several angular-loss patterns, comparing sinogram restoration, preliminary OSEM images and final refined outputs. **Section 5** summarizes our findings by analysing metrics of model performance on test dataset, and discusses limitations and directions for future improvements. **Appendices** provide additional experiments, extended qualitative results, and tables of hyperparameters used in the study.

2. Background

When two detectors measure gamma photons within a narrow time window (typically 6-12 nanoseconds), we assume they are from the same annihilation event. This paired detection forms a line of response (LOR) between the two detectors. PET systems record these events in one of two primary formats. In **list-mode data**, each coincidence is logged individually with precise identification of the detector pair and timestamp. This approach saves the maximum amount of information but generates enormous datasets. **Sinogram data** organizes coincidence events into radial, angular, and axial bins, creating a structured histogram that trades off temporal resolution for simpler processing. Standard PET scanners use 360° detector rings to achieve uniform LOR sampling, but things would be quite different when this ideal geometry isn’t possible.

Incomplete ring configurations emerge from a clash between ideal physics and practical reality. Budget constraints often drive this compromise—each detector module

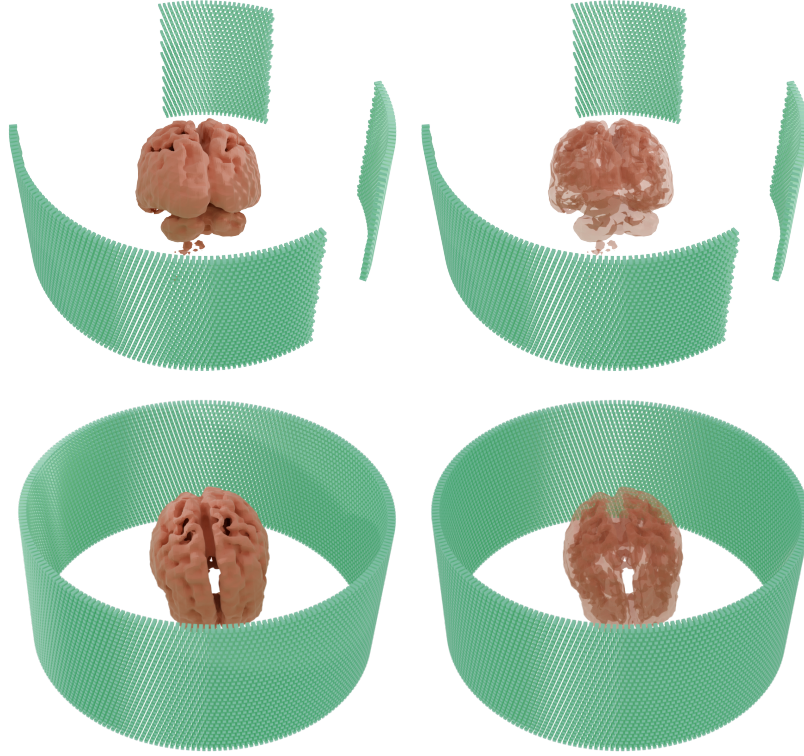


Figure 2. Three-dimensional schematic of incomplete and complete ring PET scanner detector structure, with the right image showing a perspective view.

constitutes a substantial cost, and reducing their number can make PET technology accessible to more facilities. In specialized applications, partial ring designs actually provide benefits: breast imaging benefits from closer detector positioning, interventional procedures require open scanner designs, and claustrophobic patients experience less anxiety with more open configurations.

The consequences of missing detectors are profound. LORs that would normally pass through the missing sections simply vanish from the dataset, creating angular sampling gaps. The results collapse under data deficiency if we directly reconstruct the image out of incomplete sinogram, as shown in Figure 3.

2.1. System Model and Data Simulation

To deal with these problems systematically, we made a thorough simulation framework modeling both complete and incomplete PET geometries. Our approach begins with a standard ring configuration of R axial rings (we used $R = 42$ in our experiments), each containing $D = 182$ detectors arranged cylindrically. The scanner radius (ρ) of 253.71 mm balances spatial resolution against sensitivity.

Early in our research, we attempted to use Transformer-based approaches for direct 3D image recovery, following Hatamizadeh et al.’s UNETR framework [22]. The segmentation results were excellent, but when applied to our incomplete sinogram data, these methods did not work well, with SSIM of less than 0.2 even after a long time of

training. This indicates that mere geometric information is insufficient for high-quality reconstruction when some angular segments are missing.

From listmode to sinogram, and from sinogram to reconstruction, the information is constantly losing. So, rather than attempting direct image-domain recovery, we pivoted to a two-stage method—first converting listmode data to sinograms with missing sections, then applying specialized techniques to complete these sinograms before final reconstruction. This approach, while computationally more intensive, provided a more applicable way to solve the missing data problem by retaining as much information as possible from sinogram. For simulation purposes, we mapped a $80 \times 128 \times 128$ voxel grid to physical space, yielding in-plane voxel dimensions of approximately 2.78 mm.

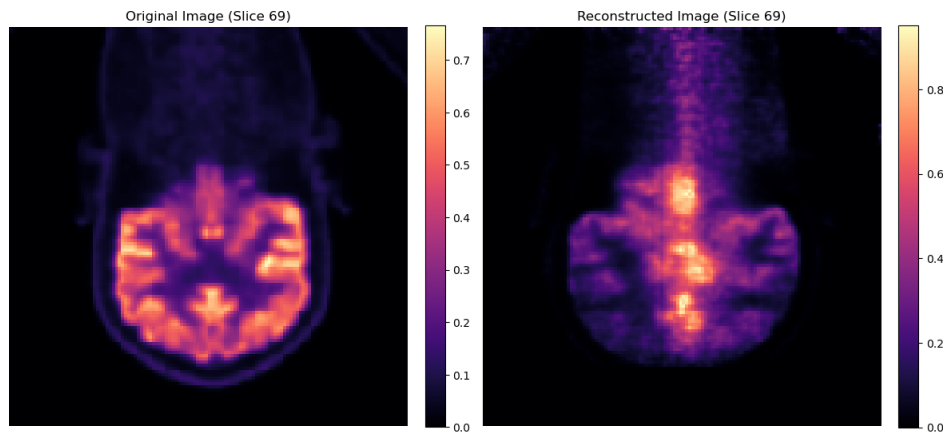


Figure 3. Comparison of reconstruction results from incomplete rings with the original image, showing that the two are vastly different, demonstrating that direct reconstruction from incomplete rings is not feasible.

The detector system itself employs a hierarchical structure with parameters that were hard to optimize. Table 1 describes some important configuration parameters of our PET system.

Our theoretical model parameters is an idealized PET system, setting aside real-world manufacturing variations that would typically require complex normalization procedures. While our framework includes parameters for TOF detection, we chose not to implement this capability in the current work, because the devices to which we intend to apply this study do not have that high temporal resolution.

Similarly, our simulation framework does not account for attenuation correction problems needing MRI or CT data in physical implementations—an important consideration for future translation of our approach. Our simulation generates idealized datasets by ray-tracing approximately 20 million emission events from $80 \times 128 \times 128$ -voxel phantom images, creating perfectly clean list-mode data without the noise and artifacts present in real-world situation. We used a dataset of 206 brain PET volumes, each with dimensions of 128^3 -voxel from a public dataset as phantom images for our simulation [23]. Each image simulates 2 billion events, the detectors detect 560 million events on average and record them in the listmode data. We then removed detectors with angles between $[30^\circ, 90^\circ]$ and $[210^\circ, 270^\circ]$. This meant that any LOR with either

Table 1. PET Scanner Configuration Parameters

Parameter	Value
Radius	253.71 mm
Crystal transaxial spacing	4.02 mm
Crystal axial spacing	5.37 mm
Module axial spacing	37.56 mm
Crystal elements (transaxial)	13
Crystal elements (axial)	7
Transaxial sectors	28
Axial sectors	1
Modules (axial)	6
Crystals per ring	364
Number of rings	42

detector within these two angular ranges cannot be recorded. Incomplete sinograms generated in this configuration only have about 306 million events, accounting for 54.6% of the originally detected events.

The complete ring configuration (Figure 2) provides our reference reconstruction \mathbf{Y}_A , representing the best-case scenario with full angular sampling. For incomplete ring experiments, we selectively remove detectors—either entire rings or angular segments—and generate a degraded reconstruction \mathbf{Y}_B from the resulting partial data. The striking quality difference between \mathbf{Y}_A and \mathbf{Y}_B shows the reconstruction challenge we aim to solve, as shown in Figure 3.

2.2. Conventional PET Reconstruction Methods

Before introducing new solutions, Several popular reconstruction approaches that are not based on machine learning have been assessed. Currently, main powerful methods are **maximum likelihood methods**, particularly MLEM and its faster variant OSEM [24], which include the Poisson statistics of photon counting. The most important parameter of these two approaches is **system model**, which relates image voxels to measured projections:

$$y_i \approx \sum_j p_{ij} \lambda_j, \quad (1)$$

Here, λ_j is the activity in voxel j , y_i is the count measured in projection i , and p_{ij} is the probability that an emission from voxel j is detected along projection i . This **system matrix** p_{ij} includes all the physics—from detector geometry to attenuation effects—that connects the unknown tracer distribution to our measurements.

MLEM iteratively updates the estimate of λ_j according to:

$$\lambda_j^{(k+1)} = \lambda_j^{(k)} \times \frac{\sum_{i=1}^N \frac{p_{ij}}{\sum_{\ell} p_{i\ell} \lambda_{\ell}^{(k)}} y_i}{\sum_{i=1}^N p_{ij}}. \quad (2)$$

However, MLEM's convergence is too slow for large datasets. OSEM makes this process faster by dividing projections into subsets and then update the image estimate using one subset at a time:

$$\lambda_j^{(k+1)} = \lambda_j^{(k)} \times \frac{\sum_{i \in S_k} \frac{p_{ij}}{\sum_{\ell} p_{i\ell} \lambda_{\ell}^{(k)}} y_i}{\sum_{i \in S_k} p_{ij}} \quad (3)$$

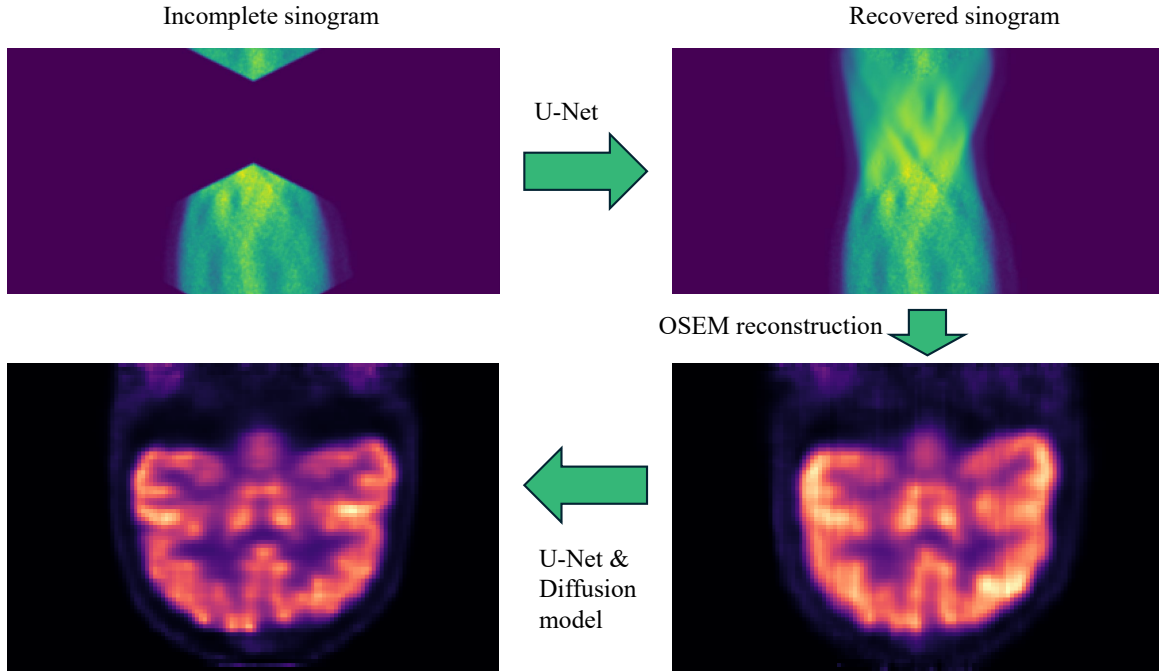


Figure 4. Overall flow diagram of the incomplete ring PET reconstruction method. First, incomplete sinograms due to missing detectors are repaired through a U-Net deep learning model to generate complete sinogram data. Then the complete sinogram is converted into a PET image using the OSEM iterative reconstruction algorithm. Finally, the image is refined using a U-Net & diffusion model to remove residual artifacts and enhance high-frequency details.

Our work mainly depends on the PyTomography library [25], which makes use of PyTorch and GPUs to make intense computations a lot faster. This technique is important when reconstructing large listmode data with around one billion events. While OSEM is powerful with full angular sampling, its performance with incomplete rings was disappointing [cf. Figure 3]. Because the missing angles also mean information loss that makes any iterative methods impossible to recover, despite their statistical

sophistication. Thus, OSEM can only be useful if the sinogram is complete or recover to a complete one. But it can not solve the core problem of missing data.

3. Methods

As shown in Figure 4, this study proposes an innovative incomplete ring PET reconstruction framework that effectively addresses the data incompleteness problem caused by missing detectors through a multi-stage strategy. In the first stage, the system first processes incomplete sinograms (top left) resulting from missing detectors, completing the missing data through a trained optimized U-Net deep learning model to generate complete sinograms (top right). This sinogram restoration process fully utilizes the five-channel input strategy, effectively integrating spatial and temporal context information.

3.1. Sinogram Reconstruction Based on Attention U-Net

Sinogram repair is very important in incomplete ring PET imaging, as its quality directly affects the precision of reconstructed images. The shape of sinogram tensors is $(D, 2D + 1, R^2)$, or $(182, 365, 1764)$ in our work, where R is the number of axial rings and D is the number of detectors each ring. And it is obvious that this tensor is too large to be directly fed into any UNet-like models. So we cut this large $(D, 2D + 1, R^2)$ tensor into $R \times (D, 2D + 1, R)$ tensors. As shown in Figure 5, the central channel of each input tensor corresponds to the current sinogram slice, while the direct spatial neighbors (slices $j - 1$ and $j + 1$) and temporal neighbors from previous and subsequent sinogram periods (slices $j - R$ and $j + R$) constitute the other four channels. For boundary handling, when adjacent indices exceed the dataset range, the central slice itself is used for channel filling, ensuring input dimension consistency. These neighboring slices are important for improving the model’s understanding of local structural continuity and temporal consistency. So finally we have $1764 \times (182, 365, 5)$ tensors for each sinogram. To make sure each image was evaluated once in the test set, we implemented 6-fold cross-validation across the 206 volumes (4 groups with 34 images and 2 groups with 35 images). The predictions obtained from our model were reconstructed using the OSEM algorithm to achieve preliminary geometric recovery, and these reconstructions were subsequently used as inputs for our second stage framework.

Although traditional U-Net performs excellently in medical image segmentation and reconstruction tasks [26], it lacks the ability to selectively focus on key features when dealing with complex incomplete ring PET sinogram restoration problems. The Attention U-Net [27] adopted in this study enhances the model’s perception of important feature regions through spatial attention mechanisms while suppressing the influence of irrelevant features, which is more useful for restoring sinograms from incomplete data. We also tested some transformer-based U-Net like UNETR [22], which combines ViT encoder and convolutional decoder, and TransUNet [28], where both encoder and

decoder are completely based on transformers. But they are slightly outperformed by Attention U-Net.

The main innovation of Attention U-Net is the introduction of attention gating (AG) modules in the skip connection path of the original U-Net. These AG modules can adaptively highlight significant structures in the feed-forward feature maps while suppressing less relevant regions. For sinogram reconstruction tasks, this mechanism is especially useful as it can selectively focus on structural features around missing areas, and then more accurately infer missing angular data. The mathematical expression of attention gating can be described as [27]:

$$\alpha_i^l = \sigma_2(\psi^T(\sigma_1(W_x^T x_i^l + W_g^T g_i + b_g)) + b_\psi), \quad (4)$$

where x_i^l is the low-level feature from the encoder, g_i is the gating signal from the decoder (high-level feature), σ_1 and σ_2 are ReLU and Sigmoid activation functions respectively, and W_x , W_g , b_g , and b_ψ are learnable parameters. $\alpha_i^l \in [0, 1]$ is the calculated attention coefficient used to control the importance of features. After processing through the attention gate, the features can be represented as:

$$\hat{x}_i^l = x_i^l \cdot \alpha_i^l. \quad (5)$$

The Attention gates learn to focus on relevant regions of the encoder feature maps by assigning weights based on the context, particularly in cases of severe angular loss. AGs can create a stronger understanding of sinogram continuity and consistency. After testing on our dataset, the results showed that Attention U-Net performs better with an average increase of 1.24dB in PSNR and 0.052 in SSIM compared to original U-Net in sinogram reconstruction tasks. This means that attention mechanism is more effective in processing incomplete ring PET data.

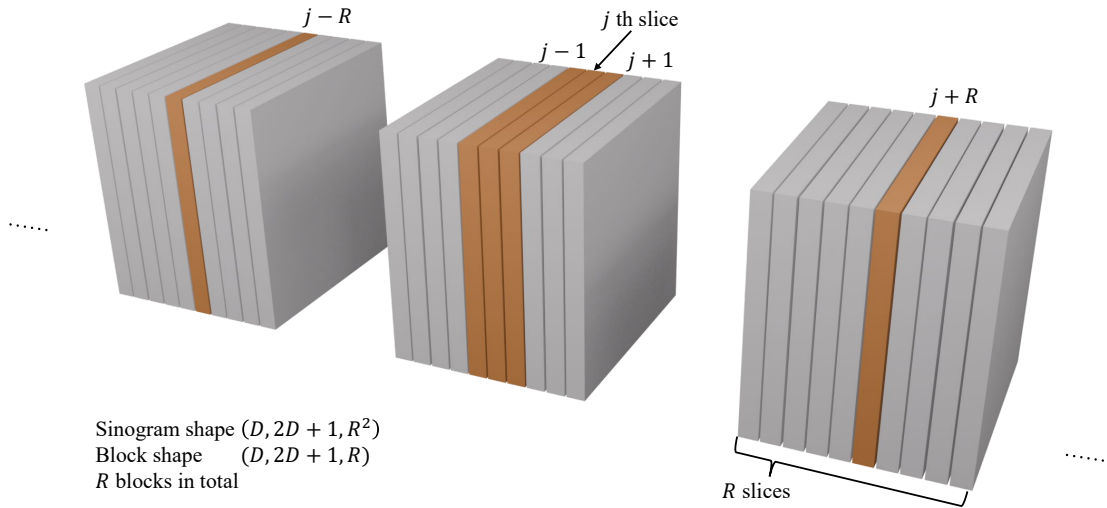


Figure 5. Visualization of the five-channel tensor preparation of sinogram data for training. Each cube represents a sinogram slice block with dimensions $(D, 2D + 1, R^2)$. The orange highlighted parts are the selected slices $(j - R, j - 1, j, j + 1, j + R)$, which form the five-channel input for the restoration model, showing the spatial and temporal relationships captured in each input tensor.

The model structure is shown in Tabel A1. Model training uses the Adam optimizer with an initial learning rate of 10^{-4} and adds 10^{-5} weight decay to prevent overfitting. Training efficiency is enhanced through mixed precision computation and gradient scaling techniques, combined with a ReduceLROnPlateau dynamic learning rate scheduler (with a decay factor of 0.3 when validation loss shows no improvement for 3 consecutive epochs), achieving stable convergence.

3.2. Image Refinement Based on U-Net and Diffusion Model

Then, to further improve the image quality in geometry space, we have the second stage of our framework, which is a dual-model architecture that combines U-Net and diffusion model. The U-Net model is used to generate a coarse prediction of the image, while the diffusion model is used to refine the image by reconstructing the residual signal. This two-stage approach effectively balances reconstruction quality with computational efficiency. Here we adopt almost the same architecture as that used in Ref. [29] except some tweaks of the hyperparameters for the training And they also use an auxiliary guidance strategy and a contrastive diffusion strategy to improve the reconstruction quality. The auxiliary guidance strategy uses neighboring axial slices and spectral information to provide additional context for the reconstruction, while the contrastive diffusion strategy ensures that the model produces anatomically plausible reconstructions specific to each individual scan. And we train the model using a combination of L1 loss and contrastive loss without pretrained weights.

3.3. Evaluation Metrics

To comprehensively evaluate the performance of the reconstruction results of both sinogram and its reconstructed images, we use several quantitative metrics. These metrics measure the similarity between reconstructed images and ground truth images from different perspectives, including pixel-level accuracy, structural fidelity, and preservation of clinically relevant features.

Peak Signal-to-Noise Ratio (PSNR) [30] is a fundamental metric for evaluating reconstructed image quality. It is calculated based on Mean Squared Error (MSE) and usually expressed on a logarithmic scale. The definition of PSNR is:

$$\text{PSNR} = 10 \cdot \log_{10} \left(\frac{\text{MAX}_I^2}{\text{MSE}} \right), \quad (6)$$

where MAX_I represents the maximum possible pixel value of the image; for images normalized to the $[0,1]$ range, $\text{MAX}_I = 1$. MSE is calculated as follows:

$$\text{MSE} = \frac{1}{mn} \sum_{i=0}^{m-1} \sum_{j=0}^{n-1} [I(i, j) - K(i, j)]^2, \quad (7)$$

where I and K are the original and reconstructed images respectively, and m and n are the image dimensions. For three-dimensional PET image voxels, the MSE calculation extends to three dimensions. PSNR values are typically expressed in decibels (dB), with

higher values indicating better reconstruction quality. In this study, PSNR values above 30dB typically indicate high-quality reconstruction

Structural Similarity Index (SSIM): Although PSNR is intuitive, it cannot adequately reflect the human visual system’s perception of structural information. SSIM addresses this deficiency by evaluating similarity in terms of brightness, contrast, and structure to more comprehensively assess image quality [31]:

$$\text{SSIM}(x, y) = \frac{(2\mu_x\mu_y + c_1)(2\sigma_{xy} + c_2)}{(\mu_x^2 + \mu_y^2 + c_1)(\sigma_x^2 + \sigma_y^2 + c_2)}, \quad (8)$$

where μ_x and μ_y are the averages of images x and y respectively; σ_x^2 and σ_y^2 are their variances; σ_{xy} is their covariance; and c_1 and c_2 are small constants set to avoid division by zero. SSIM values range between $[-1, 1]$, with 1 indicating that two images are identical. In medical image reconstruction, SSIM is particularly important because it better reflects the preservation of diagnostically relevant structures.

Normalized Mean Square Error (NMSE) normalizes the image error with respect to the energy of the original image [32]:

$$\text{NMSE} = \frac{\sum_{i,j,k} (X_{i,j,k} - \hat{X}_{i,j,k})^2}{\sum_{i,j,k} X_{i,j,k}^2}, \quad (9)$$

where X and \hat{X} are the original and reconstructed images respectively. A smaller NMSE indicates better reconstruction quality, and it is particularly useful for comparisons between different image sets and experimental setups as it eliminates the impact of image scale.

4. Results

In order to investigate the effect of the form of loss on the reconstruction results while ensuring that the total amount of data loss remained constant, we varied the range of angles at which the data were missing and ensured that the total range of missing angles remained constant and repeated the experimental procedure. The results on test set are listed in Table 2. The table includes PSNR and SSIM values of the recovered sinogram data by the first stage Attention U-Net, the reconstruction from these sinogram, and the refined images from the reconstruction using the second stage model. The results indicate that our method achieves high-quality reconstruction performance, with PSNR values exceeding 30 dB and SSIM values above 0.95 for most cases.

Figure 3 shows the comparison between directly reconstructed results without any correction and the original image. As can be seen, due to incomplete sampling caused by data loss, there are significant differences between the directly reconstructed image and the original image. These phenomena indicate that traditional PET reconstruction methods face difficulties when applied to incomplete ring PET geometries, necessitating new methods to address the data loss problem. Figure 6 demonstrates the model’s capability in reconstructing incomplete sinograms. After 40 rounds of training, the model can effectively recover complete sinogram structures from inputs with missing

Table 2. Quantitative results for different angular-loss patterns

Lost angle range	Parameter	Mean	Std
[30°, 90°] & [210°, 270°]	SSIM (refined)	0.9621	0.01251
	PSNR (refined)	30.36 dB	2.318 dB
	SSIM	0.9503	0.01480
	PSNR	29.12 dB	2.650 dB
	SSIM (sinogram)	0.9597	0.001553
	PSNR (sinogram)	35.78 dB	0.3045 dB
[60°, 120°] & [240°, 300°]	SSIM (refined)	0.9624	0.01275
	PSNR (refined)	29.97 dB	2.274 dB
	SSIM	0.9509	0.0163
	PSNR	28.91 dB	2.512 dB
	SSIM (sinogram)	0.9630	0.001632
	PSNR (sinogram)	35.91 dB	0.2762 dB
[60°, 90°] & [130°, 160°] & [240°, 260°] & [320°, 340°]	SSIM (refined)	0.9708	0.01128
	PSNR (refined)	30.92 dB	2.521 dB
	SSIM	0.9661	0.01330
	PSNR	30.10 dB	2.810 dB
	SSIM (sinogram)	0.9679	0.001341
	PSNR (sinogram)	38.41 dB	0.2695 dB

angular data. From the figure, it can be observed that although the input sinogram (left) has large-scale data loss, the model’s predicted sinogram (middle) successfully restores a structure and signal distribution highly similar to the real sinogram (right). This indicates that our proposed two-stage restoration framework can effectively learn the potential structures and features in sinograms, enabling accurate reconstruction even in cases of severe data loss. Figure 7 shows the final PET image quality generated from the reconstructed sinogram. Its PSNR reached 38.4107 dB and SSIM was 0.9679. By comparing the original PET brain image (left) with the reconstructed PET image (right), it can be seen that the reconstructed image successfully preserves key anatomical structures and tracer distribution features from the original image. Particularly in the cerebral cortex and basal ganglia regions, the reconstructed image clearly preserves the boundaries and contrast of high uptake areas.

5. Conclusion and Discussion

From the experimental results, we can confirm that our two-stage reconstruction can effectively recover PET images from incomplete ring geometries. And we also have several important findings. First, our model performs remarkably well despite operating with approximately 50% missing data and 1/3 missing detectors, in which case direct

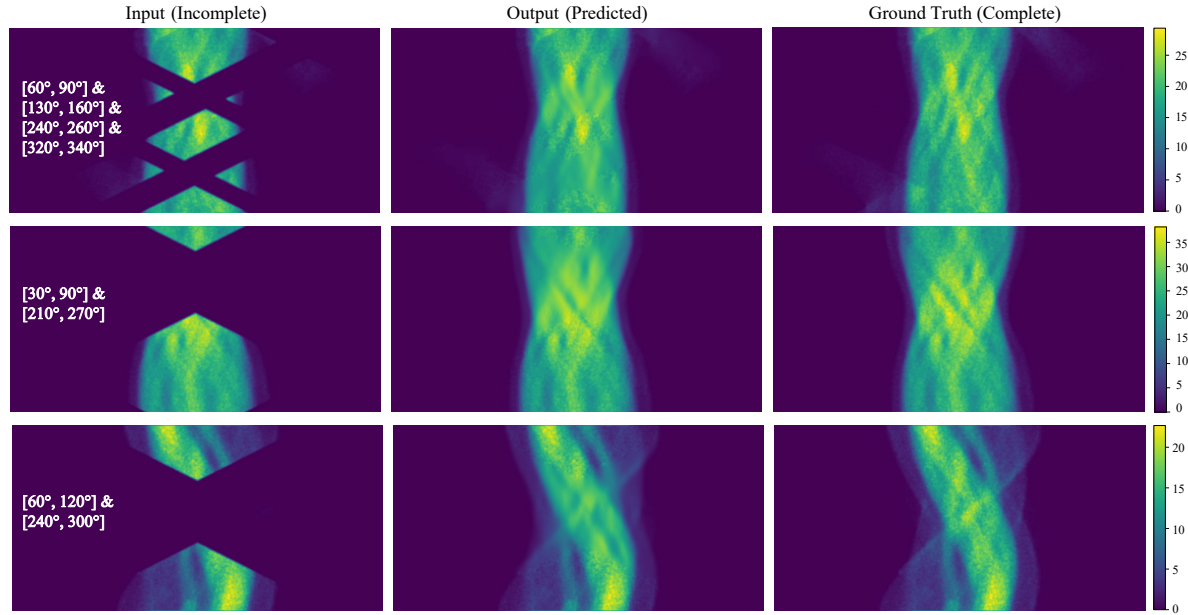


Figure 6. Comparison of PET sinogram reconstruction results after training (metrics are shown in Tabel 2). Each row displays three images: the left shows the incomplete input sinogram with missing angular data, the middle shows the model-predicted complete sinogram, and the right shows the complete real sinogram. And each row corresponds to a different angular loss range, as indicated in the first column.

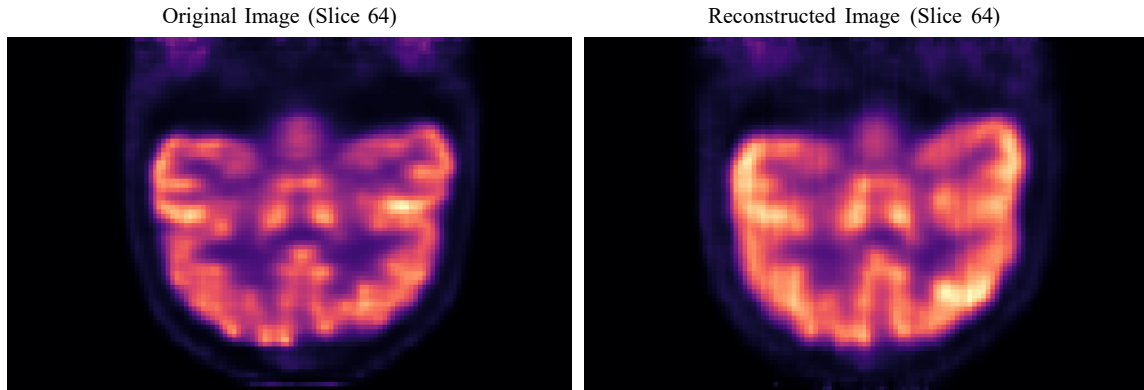


Figure 7. Comparison of original PET brain image (left) with PET image reconstructed from predicted sinogram (right), both showing the 64th layer slice with SSIM of 0.9503 and PSNR of 29.12 dB. The lost angle range is $[30^\circ, 90^\circ]$ and $[210^\circ, 270^\circ]$.

reconstruction without restoration will cause a chaos. But our approach was still able to achieve PSNR values above 30 dB and SSIM scores above 0.97 for images, indicating successful ability to recover missing information of key structural features.

While the total amount of missing data remains constant, the specific distribution of the missing affects the quality of the recovery. The model extrapolates the missing parts with the help of existing data, and when the sinogram contains an entire missing region, the model will infer the missing parts from farther away, which will lead to a decrease in the quality of recovery, as shown in the second and third rows of Figure 6.

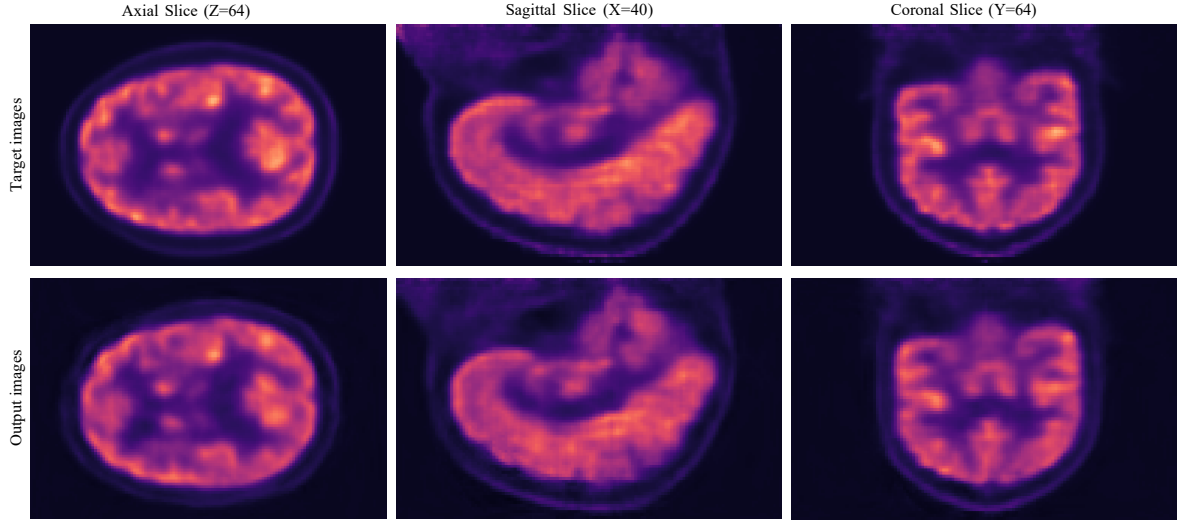


Figure 8. Comparison of original PET brain image (top) with PET image refined from the raw images reconstructed from predicted sinogram (bottom) with the SSIM of 0.9621 and PSNR of 30.36 dB. The lost angle range is $[30^\circ, 90^\circ]$ and $[210^\circ, 270^\circ]$. The axial slices should be 128×128 , but we only show the central 128×80 part.

However, when the missing and intact parts are interleaved, the quality of recovery improves because the model is able to extrapolate from a closer and thus more accurate location.

Additionally, we also found that attention mechanism is very important for the model to learn the relationship between different parts of the sinogram regardless of distances between them. Comparing the second and third rows of Figure 6, we can observe different patterns of missing data. In the third row, the missing portions are primarily concentrated in the middle region of the sinogram, with relatively balanced data preserved in both the upper and lower sections. In contrast, the second row’s missing data extends closer to the upper part of the sinogram, with only a narrow band of preserved data in the upper region. So if the model can only capture short distance relationships, obviously the second row will be more difficult to recover than the third row because the model has to extrapolate the missing parts from farther away. However, the results from Table 2 show that the PSNR and SSIM of the second row are actually quite similar to those of the third row. This indicates that the attention mechanism can help the model learn the relationship between different parts of the sinogram regardless of distances between them, which is very important for the model to leverage the existing data effectively to recover the missing parts.

Our dataset with only adjacent slices can solve the memory usage problem when processing super-large sinogram tensors in a simple way. Instead of processing the whole tensor of the size $(182, 365, 1764)$ all as a time, we divided it into $R \times (D, 2D + 1, R)$ tensors and process them sequentially. But we will lose the context for each slice. And by inputting five input channels per slice (the current slice, two spatial neighbors, and two temporal neighbors), we created a contextually sufficient representation and also lower memory costs. This approach avoid memory limitations and also enhance reconstruction

quality by considering correlated information from adjacent slices, showing an average increase of 1.24dB in PSNR and 0.052 in SSIM compared to single-slice processing.

For more robust evaluation and enough data for the second stage, we used 6-fold cross-validation on our 206 volumes dataset. This validation strategy minimizes the influence of random variation and provides more reliable performance metrics. The cross-validated results confirmed this performance advantages with PSNR of 35.6421 dB and SSIM of 0.9588 on the validation set. On the contrary, if we do not use cross validation, we can only use the data on the test set (about 36 images) for both training and testing on the model of the second stage. Because of the data leakage, the prediction on the training set cannot be used for the second stage model

Although more complex generative models like diffusion models and GANs have been used in low-dose PET reconstruction and denoising and also shown their strong capabilities in those tasks, our approach also achieves excellent results with more computationally efficient models. This is really important in clinical applications, where timely image production is essential. The SSIM values in final reconstructed images is slightly lower compared to restored sinograms, which means that some information is lost in the OSEM reconstruction. Therefore, our sinogram restoration performance is actually better than what the final image metrics show, because the OSEM reconstruction of both complete sinogram and predicted sinogram introduces their approximations, making final metrics slightly worse.

However, we still have some limitations in this study: although we adopted 2D slice processing (enhanced by adjacent slices) to improve memory efficiency, a fully 3D version might perform better as it has a more comprehensive context of sinogram. Or we can also try to use recurrent neural network or attention mechanism to capture more precise relationships between difference slices. Additionally, we are mainly validating for ring-type and partial angular coverage, but missing detectors in real-world situation might lead to more complex missing patterns, requiring more advanced geometric modeling methods.

Looking toward future improvements, positional encoding could also be incorporated to better account for the sequential nature of axial slices. Additionally, while we tested transformer-based architectures like UNETR and TransUNet, they were slightly outperformed by Attention U-Net in our specific task. Therefore, for our current dataset size, convolutional architectures remains beneficial. However, if we can have larger datasets, transformer-based approaches might fulfil their full potential.

6. Acknowledgments

I would like to express my sincere gratitude to senior students, Xiaoyu Chen for insightful discussions and suggestions. The conclusions and analyses presented in this publication were produced using the following software: Python (Guido van Rossum 1986) [33], Opencv (Intel, Willow Garage, Itseez) [34], Scipy (Jones et al. 2001) [35], PyTorch (Meta AI September 2016) [36], Matplotlib (Hunter 2007) [37] and Seaborn [38]. The dataset

for this study can be found in <https://github.com/Show-han/PET-Reconstruction.git>.

Appendix A. Parameters of models

The parameters of the five-channel U-Net network structure are shown in Table A1. We also have skip connections between the encoder and decoder blocks, which are not shown in the table.

Table A1. Five-channel Attention U-Net backbone

Stage / block(s)	Main ops (per level)	C_{out}
Input	—	5
Encoder $\times 4$	[Conv 3×3 + BN + ReLU] $\times 2$ MaxPool 2×2	64, 128, 256, 512
Bottleneck	[Conv 3×3 + BN + ReLU] $\times 2$	1024
Decoder $\times 4$	Upsample ($\uparrow 2$) + skip concat [Conv 3×3 + BN + ReLU] $\times 2$	512, 256, 128, 64
Output	Conv 1×1	5

All hyperparameters required to replicate the run are collected in Table Appendix A.

Table A2. Numerical hyper-parameters for the stage-2 run

Hyper-parameter	Value	Hyper-parameter	Value
<i>Data</i>		<i>Channel multipliers</i>	
batch_size	12	levels	1, 2, 3, 4
l_resolution (=r)	64	<i>Diffusion process</i>	
<i>U-Net</i>		image_size	128
in_channel	1	T_{train}	2 000
out_channel	1	T_{val}	10
inner_channel	64	β_{start}	1×10^{-6}
res_blocks	3	$\beta_{\text{end,train}}$	0.01
<i>diffusion model</i>		$\beta_{\text{end,val}}$	0.5
in_channel	2	<i>Optimisation</i>	
out_channel	1	n_iter	600 000
inner_channel	32	learning rate	0.0002
res_blocks	3	EMA decay	0.9999

References

- [1] David W. Townsend, Jonathan P. J. Carney, Jeffrey T. Yap, and Nathan C. Hall. PET/CT today and tomorrow. *Journal of Nuclear Medicine*, 45(1 Suppl):4S–14S, 2004.
- [2] Gerd Muehllehner and Joel S Karp. Positron emission tomography. *Physics in Medicine & Biology*, 51(13):R117, 2006.
- [3] Katherine Lameka, Michael D Farwell, and Masanori Ichise. Positron emission tomography. *Handbook of clinical neurology*, 135:209–227, 2016.
- [4] Arvind K Shukla and Utham Kumar. Positron emission tomography: An overview. *Journal of medical physics*, 31(1):13–21, 2006.
- [5] Ronald Nutt. The history of positron emission tomography. *Molecular Imaging & Biology*, 4(1):11–26, 2002.
- [6] Suleman Surti and Joel S. Karp. Design considerations for a limited-angle, dedicated breast TOF-PET scanner. *Physics in Medicine and Biology*, 53(11):2911–2921, 2008.
- [7] Hideaki Tashima, Takatomo Yamaya, Eri Yoshida, Shingo Kinouchi, Masaaki Watanabe, and Eiji Tanaka. A single-ring OpenPET enabling PET imaging during radiotherapy. *Physics in Medicine and Biology*, 57(14):4705–4718, 2012.
- [8] Sangeetha Krishnamoorthy, Boon-Keng K. Teo, Wei Zou, James McDonough, Joel S. Karp, and Suleman Surti. A proof-of-concept study of an in-situ partial-ring time-of-flight PET scanner for proton beam verification. *IEEE Transactions on Radiation and Plasma Medical Sciences*, 5(5):694–702, 2021.
- [9] Hengquan Zhang, Yuli Wang, Jinyi Qi, and Shiva Abbaszadeh. Penalized maximum-likelihood reconstruction for improving limited-angle artifacts in a dedicated head and neck PET system. *Physics in Medicine and Biology*, 65(16):165016, 2020.
- [10] Avinash C. Kak and Malcolm Slaney. *Principles of Computerized Tomographic Imaging*. IEEE Press, 1988.
- [11] Jinyi Qi and Richard M. Leahy. Iterative reconstruction techniques in emission computed tomography. *Physics in Medicine and Biology*, 51(15):R541–R578, 2006.
- [12] Shubhangi Makkar, Siqi Ye, Marina Béguin, Günther Dissertori, Jan Hrbacek, Antony Lomax, Keegan McNamara, Christian Ritzer, Damien C. Weber, Lei Xing, and Carla Winterhalter. Partial-ring PET image correction using implicit neural representation learning. In *XXth International Conference on the use of Computers in Radiation therapy*, Lyon, France, July 2024. 8–11 July 2024.
- [13] Yeqi Fang, Wei Hong, and Jun Tao. Identifying black holes through space telescopes and deep learning. *Phys. Rev. D*, 110:063011, Sep 2024.
- [14] Chang Liu, Yeqi Fang, YuHuan Xie, Hao Zheng, Xin Li, Dongsheng Wu, and Tao Zhang. Deep learning pneumoconiosis staging and diagnosis system based on multi-stage joint approach. *BMC Medical Imaging*, 24(165), jul 2024.
- [15] Andrew J Reader, Guillaume Corda, Abolfazl Mehranian, Casper da Costa-Luis, Sam Ellis, and Julia A Schnabel. Deep learning for pet image reconstruction. *IEEE Transactions on Radiation and Plasma Medical Sciences*, 5(1):1–25, 2020.
- [16] V. S. S. Kandarpa, Alexandre Bousse, Didier Benoit, and Dimitris Visvikis. Dug-recon: A framework for direct image reconstruction using convolutional generative networks. *IEEE Transactions on Radiation and Plasma Medical Sciences*, 5(1):44–53, January 2021.
- [17] Cheng-Cheng Liu and Hsiu-Maan Huang. Partial-ring PET image restoration using a deep learning based method. *Physics in Medicine and Biology*, 64(22):225014, 2019.
- [18] Yuxin Xue, Yige Peng, Lei Bi, Dagan Feng, and Jinman Kim. Cg-3dsrgan: A classification guided 3d generative adversarial network for image quality recovery from low-dose pet images, 2023.
- [19] Andrew J. Reader and Bo Pan. Artificial intelligence for PET image reconstruction. *British Journal of Radiology*, 96(1150):20230292, 2023.
- [20] Rajat Vashistha, Viktor Vegh, Hamed Moradi, Amanda Hammond, Kevin O’Brien, and David

- Reutens. Modular GAN: PET image reconstruction using two generative adversarial networks. *Frontiers in Radiology*, 4:1466498, 2024.
- [21] Felix Neumaier, Boris Zlatopolskiy, and Bernd Neumaier. Mutated isocitrate dehydrogenase (midh) as target for pet imaging in gliomas. *Molecules*, 28:2890, 03 2023.
- [22] Ali Hatamizadeh, Yucheng Tang, Vishwesh Nath, Dong Yang, Andriy Myronenko, Bennett Landman, Holger Roth, and Daguang Xu. Unetr: Transformers for 3d medical image segmentation, 2021.
- [23] Zeyu Han, Yuhan Wang, Peng Wang, Binyu Yan, Yan Wang, Luping Zhou, Jiliu Zhou, and Dinggang Shen. Contrastive diffusion model with auxiliary guidance for coarse-to-fine pet reconstruction. In *Medical Image Computing and Computer-Assisted Intervention – MICCAI 2023, LNCS*, volume 14229, pages 239–249. Springer, Cham, 2023.
- [24] H.M. Hudson and R.S. Larkin. Accelerated image reconstruction using ordered subsets of projection data. *IEEE Transactions on Medical Imaging*, 13(4):601–609, 1994.
- [25] Lucas A. Polson, Roberto Fedrigo, Chenguang Li, Maziar Sabouri, Obed Dzikunu, Shadab Ahamed, Nicolas Karakatsanis, Sara Kurkowska, Peyman Sheikhzadeh, Pedro Esquinas, Arman Rahmim, and Carlos Uribe. Pytomography: A python library for medical image reconstruction. *SoftwareX*, 29:102020, 2025.
- [26] Olaf Ronneberger, Philipp Fischer, and Thomas Brox. U-net: Convolutional networks for biomedical image segmentation, 2015.
- [27] Ozan Oktay, Jo Schlemper, Loic Le Folgoc, Matthew Lee, Mattias Heinrich, Kazunari Misawa, Kensaku Mori, Steven McDonagh, Nils Y Hammerla, Bernhard Kainz, Ben Glocker, and Daniel Rueckert. Attention u-net: Learning where to look for the pancreas, 2018.
- [28] Jieneng Chen, Yongyi Lu, Qihang Yu, Xiangde Luo, Ehsan Adeli, Yan Wang, Le Lu, Alan L. Yuille, and Yuyin Zhou. Transunet: Transformers make strong encoders for medical image segmentation, 2021.
- [29] Zeyu Han, Yuhan Wang, Luping Zhou, Peng Wang, Binyu Yan, Jiliu Zhou, Yan Wang, and Dinggang Shen. Contrastive diffusion model with auxiliary guidance for coarse-to-fine PET reconstruction. In *Medical Image Computing and Computer Assisted Intervention – MICCAI 2023, LNCS*, pages 239–249. Springer, 2023.
- [30] Alain Horé and Djemel Ziou. Image quality metrics: Psnr vs. ssim. In *Proc. 20th International Conference on Pattern Recognition (ICPR)*, pages 2366–2369. IEEE, 2010.
- [31] Zhou Wang, Alan C. Bovik, Hamid R. Sheikh, and Eero P. Simoncelli. Image quality assessment: from error visibility to structural similarity. *IEEE Trans. Image Process.*, 13(4):600–612, 2004.
- [32] Shigeaki Higashiyama, Yutaka Katayama, Atsushi Yoshida, Nahoko Inoue, Takashi Yamanaga, Takao Ichida, Yukio Miki, and Joji Kawabe. Investigation of the effectiveness of no-reference metric in image evaluation in nuclear medicine. *PLOS ONE*, 19(11):e0310305, 2024.
- [33] Guido Van Rossum and Fred L. Drake. *Python 3 Reference Manual*. CreateSpace, Scotts Valley, CA, 2009.
- [34] Itseez. Open source computer vision library. <https://github.com/itseez/opencv>, 2015.
- [35] Pauli Virtanen, Ralf Gommers, Travis E. Oliphant, Matt Haberland, Tyler Reddy, David Cournapeau, Evgeni Burovski, Pearu Peterson, Warren Weckesser, Jonathan Bright, Stéfan J. van der Walt, Matthew Brett, Joshua Wilson, K. Jarrod Millman, Nikolay Mayorov, Andrew R. J. Nelson, Eric Jones, Robert Kern, Eric Larson, C J Carey, İlhan Polat, Yu Feng, Eric W. Moore, Jake VanderPlas, Denis Laxalde, Josef Perktold, Robert Cimrman, Ian Henriksen, E. A. Quintero, Charles R. Harris, Anne M. Archibald, Antônio H. Ribeiro, Fabian Pedregosa, Paul van Mulbregt, and SciPy 1.0 Contributors. SciPy 1.0: Fundamental Algorithms for Scientific Computing in Python. *Nature Methods*, 17:261–272, 2020.
- [36] Adam Paszke, Sam Gross, Francisco Massa, Adam Lerer, James Bradbury, Gregory Chanan, Trevor Killeen, Zeming Lin, Natalia Gimelshein, Luca Antiga, Alban Desmaison, Andreas Kopf, Edward Yang, Zachary DeVito, Martin Raison, Alykhan Tejani, Sasank Chilamkurthy, Benoit Steiner, Lu Fang, Junjie Bai, and Soumith Chintala. Pytorch: An imperative style, high-

- performance deep learning library. In *Advances in Neural Information Processing Systems 32*, pages 8024–8035. Curran Associates, Inc., 2019.
- [37] J. D. Hunter. Matplotlib: A 2d graphics environment. *Computing in Science & Engineering*, 9(3):90–95, 2007.
- [38] Michael L. Waskom. seaborn: statistical data visualization. *Journal of Open Source Software*, 6(60):3021, 2021.
- [39] Mengwei Ren, Mauricio Delbracio, Hossein Talebi, Guido Gerig, and Peyman Milanfar. Multiscale structure guided diffusion for image deblurring. *arXiv preprint arXiv:2212.01789*, 2022. Accessed: 2025-01-20.
- [40] Chitwan Saharia, Jonathan Ho, William Chan, Tim Salimans, David J. Fleet, and Mohammad Norouzi. Image super-resolution via iterative refinement. *IEEE Transactions on Pattern Analysis and Machine Intelligence*, 2022. Accessed: 2025-01-20.
- [41] Ye Zhu, Yu Wu, Kyle Olszewski, Jian Ren, Sergey Tulyakov, and Yan Yan. Discrete contrastive diffusion for cross-modal and conditional generation. *arXiv preprint arXiv:2206.07771*, 2022. Accessed: 2025-01-20.
- [42] Ida Häggström, Charles R. Schmidtlein, Gabriel Campanella, and Thomas J. Fuchs. DeepPET: A deep encoder-decoder network for direct PET image reconstruction. *Medical Image Analysis*, 54:253–262, 2019. Accessed: 2025-01-20.
- [43] Ying Wang, Lei Zhou, Biao Yu, Li Wang, Chao Zu, David S. Lalush, Weili Lin, Xiaoping Wu, Jiliu Zhou, and Dinggang Shen. 3d conditional generative adversarial networks for high-quality PET image estimation at low dose. *NeuroImage*, 174:550–562, 2018. Accessed: 2025-01-20.
- [44] Biao Yu, Lei Zhou, Li Wang, Feng Shi, Jurgen Fripp, and Pierrick Bourgeat. Ea-gans: Edge-aware generative adversarial networks for cross-modality MR image synthesis. *IEEE Transactions on Medical Imaging*, 38(7):1750–1762, 2019. Accessed: 2025-01-20.
- [45] Yating Luo, Lei Zhou, Bo Zhan, Yanan Fei, Jiliu Zhou, Ying Wang, and Dinggang Shen. Adaptive rectification based adversarial network with spectrum constraint for high-quality PET image synthesis. *Medical Image Analysis*, 77:102335, 2022. Accessed: 2025-01-20.
- [46] Peipei Zeng, Lei Zhou, Chao Zu, Xiaoyun Zeng, Zonglei Jiao, Xiaoping Wu, Jiliu Zhou, Dinggang Shen, and Ying Wang. 3d cvt-gan: A 3d convolutional vision transformer-gan for PET reconstruction. In *Medical Image Computing and Computer Assisted Intervention – MICCAI 2022*, pages 516–526, 2022. Accessed: 2025-01-20.
- [47] Arash Vahdat and Jan Kautz. Nvae: A deep hierarchical variational autoencoder. In *Advances in Neural Information Processing Systems (NeurIPS)*, 2020. Accessed: 2025-01-20.
- [48] Jonathan Ho, Ajay Jain, and Pieter Abbeel. Denoising diffusion probabilistic models, 2020.
- [49] Jascha Sohl-Dickstein, Eric Weiss, Niru Maheswaranathan, and Surya Ganguli. Deep unsupervised learning using nonequilibrium thermodynamics. In Francis Bach and David Blei, editors, *Proceedings of the 32nd International Conference on Machine Learning*, volume 37 of *Proceedings of Machine Learning Research*, pages 2256–2265, Lille, France, 07–09 Jul 2015. PMLR.
- [50] Qing Shan, Jianqi Wang, and Dong Liu. Deep image prior-based PET reconstruction from partial data. *IEEE Transactions on Radiation and Plasma Medical Sciences*, 8(4):416–425, 2024.
- [51] George Webber and Andrew J. Reader. Diffusion models for medical image reconstruction. *British Journal of Radiology — Artificial Intelligence*, 1(1), 2024.
- [52] Imraj R. D. Singh, Alexander Denker, Riccardo Barbano, Željko Kereta, Bangti Jin, Kris Thielemans, Peter Maass, and Simon R. Arridge. Score-based generative models for PET image reconstruction. *Machine Learning for Biomedical Imaging (MELBA)*, 2, 2024.
- [53] Kuang Gong, Keith A. Johnson, Georges El Fakhri, Quanzheng Li, and Tinsu Pan. PET image denoising based on denoising diffusion probabilistic model. *European Journal of Nuclear Medicine and Molecular Imaging*, 51(2):358–368, 2024.
- [54] Chitwan Saharia, Jonathan Ho, William Chan, Tim Salimans, David J. Fleet, and Mohammad Norouzi. Image super-resolution via iterative refinement. *IEEE Transactions on Pattern Analysis and Machine Intelligence*, 2023.

- [55] Huidong Xie, Weijie Gan, Bo Zhou, and *et al.*. Dose-aware diffusion model for 3d low-dose PET: multi-institutional validation with reader study and real low-dose data. *arXiv preprint arXiv:2405.12996*, 2024.
- [56] Seyedehsamaneh Shojaeilangari, Clinton R. Schmitzlein, Arman Rahmim, and Mohammad R. Ay. Recovery of missing data in partial geometry pet scanners: Compensation in projection space vs image space. *Medical Physics*, 45(12):5437–5449, 2018.
- [57] Chih-Chieh Liu and Hsuan-Ming Huang. Partial-ring pet image restoration using a deep learning based method. *Phys. Med. Biol.*, 64(22):225014, 2019.
- [58] Zhendong Wang, Xiaodong Cun, Jianmin Bao, Wengang Zhou, Jianzhuang Liu, and Houqiang Li. Uformer: A general u-shaped transformer for image restoration, 2021.
- [59] Dinggang Shen, Guorong Wu, and Heung-Il Suk. Deep learning in medical image analysis. *Annual review of biomedical engineering*, 19(1):221–248, 2017.